Magnetic Resonance Imaging 63 (2019) 258–266

Contents lists available at ScienceDirect

Magnetic Resonance Imaging

journal homepage: www.elsevier.com/locate/mri

Original contribution

Automated gradient-based electrical properties tomography in the human brain using 7 Tesla MRI

Yicun Wang[a], Pierre-Francois Van de Moortele[b], Bin He[c,*]

[a] Department of Biomedical Engineering, University of Minnesota, Minneapolis, MN 55455, USA
[b] Center for Magnetic Resonance Research, University of Minnesota, Minneapolis, MN 55455, USA
[c] Department of Biomedical Engineering, Carnegie Mellon University, PA 15213, USA

ARTICLE INFO

Keywords:
Magnetic resonance based electrical properties tomography
B_1 mapping
7 T MRI
Human brain
Electrical properties
Quantitative imaging

ABSTRACT

Electrical properties of the brain tissues may yield useful biomarkers for neurological disorders and diseases, as well as contribute to safety assurance of ultra-high-field MRI. It has been reported that using B_1 maps from a multi-channel RF coil, the spatial variation of the electrical properties can be robustly retrieved. The absolute electrical property values can then be obtained by spatial integration, given that an integration seed point is assigned. In this study, we propose to exploit automatically detected seed points based on tissue piece-wise homogeneity (Helmholtz equation) for spatial integration. Numerical simulations of a numerical brain model and experiments involving 12 healthy volunteers were performed to demonstrate its feasibility and robustness in various noisy conditions and head positions. For *in vivo* imaging, we consistently observed higher conductivity and permittivity values in the white and gray matter compared to tabulated *ex vivo* probe measurement results found in the literature, a discrepancy that may be attributed to *ex vivo* experimental constraints. Our results suggest that the proposed technique produces consistent brain electrical properties *in vivo* that may contribute to improving diagnostic and therapeutic decisions.

1. Introduction

Electrical properties (EPs) comprise electrical conductivity and permittivity. They are determined by the constituents and the hierarchical organization of the tissue and vary as functions of frequency [1,2]. Non-invasive EP imaging technologies are based on Maxwell's equations with various degree of simplifications which take account of the operating frequency and the imaging hardware. Electrical Impedance Tomography (EIT) and Magnetic Resonance based Electrical Impedance Tomography (MREIT) require low-frequency (< 1 kHz) electrical currents to be injected into the imaged structure, and the perturbed surface voltage or magnetic field are measured to infer the underlying EPs [3–6]. Magneto-Acoustic Tomography with Magnetic Induction (MAT-MI) retrieves tissue conductivity at ultrasound frequency (~2MHz) based on inductive current and Lorentz force [7,8]. Microwave imaging uses the scattering matrix of an antenna array to retrieve the underlying tissue conductivity and permittivity [9]. However, these technologies are limited by either low spatial resolution or applicability to brain imaging *in vivo*.

Magnetic Resonance based Electrical Properties Tomography (MREPT or EPT) is an imaging modality for measuring tissue EPs at radiofrequency (RF) which recently received considerable attention [10–14]. EPT central equations relate EPs with MRI-measurable RF field, or B_1 field. Previous studies have demonstrated its potentials to produce biomarkers for diseases such as cancer [15–17]. With the advent of ultra-high field MRI, MREPT is receiving increased interest as the retrieved subject-specific EPs could be used for local specific absorption rate (SAR) estimation and RF safety assurance [11,18].

Gradient-based EPT (gEPT) is an EPT technology tailored for multi-channel transceiver RF arrays [19], which has demonstrated promise for brain EP imaging. In contrast to the conventional approach based on tissue piece-wise homogeneity assumption, gEPT preserves correct EP contrast on tissue boundaries by explicitly reconstructing the spatial variation or “gradient” of tissue EPs, followed by spatial integration from a user-assigned seed point as ground truth. The EPs of the seed point are assigned according to *ex vivo* measurement of biological tissues from Gabriel et al. 1996 [20]. Therefore, the reconstruction accuracy is dependent on the subjective choice of seed points, which presents a major challenge to its clinical applicability.

In this study, we propose a novel strategy to assign seed points for gEPT automatically. Seed EPs calculated from B_1 maps measured *in vivo* were used instead of the tabulated *ex vivo* values. We performed

* Corresponding author at: Department of Biomedical Engineering, Carnegie Mellon University.
E-mail address: bhe1@andrew.cmu.edu (B. He).

https://doi.org/10.1016/j.mri.2019.08.003
Received 3 June 2019; Received in revised form 1 August 2019; Accepted 15 August 2019

numerical simulations and human experiments involving 12 healthy subjects at 7 T to quantitatively evaluate the performance of the method. In addition, we summarized literature EPT results in the human brain to provide an overview of the consistency and differences among them, and to compare them with the *ex vivo* probe measurement values.

2. Material and methods

2.1. Theoretical background

MRI relies on RF magnetic field to interact with the spin system under detection. The transmit RF wave has a relatively narrow bandwidth, typically a few kHz, centered at the proton resonance frequency (Larmor frequency) usually between several tens and several hundreds of MHz. Since EP variation is negligible across this frequency band, one can simplify the magnetic field $\overrightarrow{B}$ as a single frequency and express it using a complex phasor term. The pattern of this complex field is mainly determined by the RF coil, but it is also significantly influenced by the EPs of the underlying imaged structure, as dictated by Maxwell's equations. Therefore, given measurements of $\overrightarrow{B}$, an inverse problem can be established to infer EP distributions.

In an MRI experiment, $\overrightarrow{B}$ cannot be directly measured, but rather its counter-rotating components in the transverse plane, defined as $B_{1,rot}^{+} = \frac{B_x + iB_y}{2}$ and $B_{1,rot}^{-} = \left(\frac{B_x - iB_y}{2}\right)^*$, respectively [21], where $*$ denotes complex conjugate. These two quantities are known as the transmit and receive sensitivity of a RF coil. In this work, we define

$$B_1^+ = |B_1^+|\ e^{i\varphi^+} := \frac{B_x + iB_y}{2} = B_{1,rot}^+ \tag{1}$$

$$B_1^- = |B_1^-|\ e^{i\varphi^-} := \frac{B_x - iB_y}{2} = B_{1,rot}^{-*} \tag{2}$$

$B_{1,rot}^{-*}$ is used instead of $B_{1,rot}^{-}$ since the former directly contributes to the MR signal equation. Assuming that the magnetic susceptibility in the brain tissue can be approximated by μ_0, and that the spatial variation of B_z is negligible [19,22], one can derive from Maxwell's equations that

$$\nabla^2 B_1^+ \approx -\omega^2\mu_0\varepsilon_c B_1^+ + \left(\frac{\partial B_1^+}{\partial x} - i\frac{\partial B_1^+}{\partial y}\right)g_+ + \frac{\partial B_1^+}{\partial z}g_z \tag{3}$$

$$\nabla^2 B_1^- \approx -\omega^2\mu_0\varepsilon_c B_1^- + \left(\frac{\partial B_1^-}{\partial x} + i\frac{\partial B_1^-}{\partial y}\right)g_- + \frac{\partial B_1^-}{\partial z}g_z. \tag{4}$$

where $\varepsilon_c := \varepsilon_r\varepsilon_0 - i\sigma/\omega$ is the complex electrical properties (ε_r denotes relative permittivity to vacuum permittivity ε_0, and σ denotes conductivity in S/m); $g_\pm := (\partial/\partial x \pm i\,\partial/\partial y)\,ln\,\varepsilon_c$, $g_z := (\partial/\partial z)\,ln\,\varepsilon_c$.

Despite the availability of B_1 magnitude by a wide selection of B_1 mapping methods, a critical challenge for EPT is the absence of the absolute phase information from both $B_1{}^+$ and $B_1{}^-$. For cases where a quadrature coils is used at magnetic field lower than 3 T, it is observed that $\angle B_1{}^+ \approx \angle B_1{}^-$ [23]. Based on this observation, the signal phase acquired using sequences unsensitized to magnetic susceptibility, such as turbo spin echo or steady state free procession, can be exploited to estimate the absolute RF phase [24,25]. Alternatively, the unknown phase information can be considered as an additional variable in the equation and solved simultaneously with EPs [19,26,27]. The latter leads to a higher dimension of solution space, and as a result multiple B_1 distributions are required to achieve a reliable solution.

2.2. gEPT as a voxel-wise inverse problem

Consider a multi-channel RF coil array with P transmit elements and Q receive elements. Define relative B_1 as the B_1 magnitude of a single channel with relative phase to an arbitrarily selected channel r. By taking relative phase between channels, their shared phase terms irrelevant to RF field can be eliminated, such as those induced from chemical shift, B_0 heterogeneity and eddy current effects.

$$B_{1pr}^+ = |B_{1p}^+|\ e^{i(\varphi_p^+ - \varphi_r^+)} = |B_{1p}^+|\ e^{i\varphi_{pr}^+} \tag{5}$$

$$B_{1qr}^- = |B_{1q}^-|\ e^{i(\varphi_q^- - \varphi_r^-)} = |B_{1q}^-|\ e^{i\varphi_{qr}^-} \tag{6}$$

Introducing Eqs. (5) and (6) to (3) and (4), respectively, we have pixel-wise inverse problems

$$\begin{bmatrix} B_{1pr}^+ \\ \frac{\partial B_{1pr}^+}{\partial x} \\ \frac{\partial B_{1pr}^+}{\partial y} \\ \frac{\partial B_{1pr}^+}{\partial z} \end{bmatrix}^{\mathrm{T}} \cdot \begin{bmatrix} \omega^2\mu_0\varepsilon_c + i\nabla^2\varphi_r^+ - \|\nabla\varphi_r^+\|^2 - i\left(\frac{\partial\varphi_r^+}{\partial x} - i\frac{\partial\varphi_r^+}{\partial y}\right)g_+ - i\frac{\partial\varphi_r^+}{\partial z}g_z \\ 2i\frac{\partial\varphi_r^+}{\partial x} - g_+ \\ 2i\frac{\partial\varphi_r^+}{\partial y} + ig_+ \\ 2i\frac{\partial\varphi_r^+}{\partial z} - g_z \end{bmatrix} = -\nabla^2 B_{1pr}^+ \tag{7}$$

$$\begin{bmatrix} B_{1qr}^- \\ \frac{\partial B_{1qr}^-}{\partial x} \\ \frac{\partial B_{1qr}^-}{\partial y} \\ \frac{\partial B_{1qr}^-}{\partial z} \end{bmatrix}^{\mathrm{T}} \cdot \begin{bmatrix} \omega^2\mu_0\varepsilon_c + i\nabla^2\varphi_r^- - \|\nabla\varphi_r^-\|^2 - i\left(\frac{\partial\varphi_r^-}{\partial x} + i\frac{\partial\varphi_r^-}{\partial y}\right)g_- - i\frac{\partial\varphi_r^-}{\partial z}g_z \\ 2i\frac{\partial\varphi_r^-}{\partial x} - g_- \\ 2i\frac{\partial\varphi_r^-}{\partial y} - ig_- \\ 2i\frac{\partial\varphi_r^-}{\partial z} - g_z \end{bmatrix} = -\nabla^2 B_{1qr}^- \tag{8}$$

where T denotes vector transpose. Eqs. (7) and (8) can be solved for g_+ and $\nabla\varphi_r{}^+$, as well as g_- and $\nabla\varphi_r{}^-$, given that $P > 4$ and $Q > 4$ [19,28,29]. In this study, we used a 16-channel transceiver array operating in single-channel mode, rendering $P = Q = 16$.

2.3. Automated seed selection

EP seeds are voxels selected to have presumptive EP values. Since Eqs. (7) and (8) only yield EPs gradient, assignment of seeds is imperative to retrieve absolute EP distributions. In the original gEPT work [19], a single seed is manually selected in the putamen on T_1-weighted images and assigned EPs of gray matter based on the tabulated *ex vivo* measurement results [20]. In this study, by contrast, we calculate local EP values based on the Helmholtz equation

$$\varepsilon_{c,local} = -\frac{\nabla^2 B_1^+}{\omega^2\mu_0 B_1^+} = -\frac{2i\nabla\varphi^+\cdot\nabla|B_1^+| - (\nabla\varphi^+\cdot\nabla\varphi^+)|B_1^+| + \nabla^2|B_1^+| + i\,|B_1^+|\nabla^2\varphi^+}{\omega^2\mu_0|B_1^+|} \tag{9}$$

using measured $|B_1{}^+|$ and retrieved $\nabla\varphi^+$ in the previous step. It is well known that using the Helmholtz equation alone results in artifacts in transition zones with spatial variations of EP values [30,31], however, we hypothesized that multiple brain areas are locally sufficiently homogeneous to be immune from significant biases of this kind. These local areas can be detected by their smaller EP gradient strength calculated from the Helmholtz equation. A specific number of such areas, together with their EPs, can be used as a L_2-norm regularization term to the gradient consistency terms

$$\min_{\Theta}\ \|D_x\Theta - g_x\|^2 + \|D_y\Theta - g_y\|^2 + \lambda\ \|\Theta_n - \Theta_0\|^2 \tag{10}$$

where Θ is a vector of $ln\varepsilon_c$ inside ROI; D_x and D_y are the spatial finite difference operator along x and y directions, respectively; Θ_n vector represents N seed points selected and Θ_0 is their calculated EP values from the local equation; λ is the regularization parameter determining

how "trustworthy" the selected seeds are. In this study, λ is empirically chosen as 0.45. Notably, the original gEPT integration is a special case of this central equation with a fixed Θ_0, $N = 1$ and $\lambda \gg 1$. Implementation details of the algorithm for brain imaging is provided in the "image reconstruction" subsection.

2.4. Numerical simulations

Electromagnetic simulations were performed in SEMCAD X (Schmid & Partner Engineering AG, Zurich, Switzerland). The 16-channel stripline RF transceivers used in the experiment [32] was numerically constructed and loaded with the Ella model in Virtual Family [33]. The model was truncated below the shoulder to alleviate computational load. The head model was first positioned supine in the coil, then rotated around the central z-axis by 15° to disrupt the left-right symmetry, an assumption used and explained in the "image reconstruction" subsection. Automatic discretization was performed by the software based on the material and geometry of the enclosed structures. The RF coil was simulated as a 16-port network, with one channel played at a time while others terminated with 50 Ω. The simulated fields were interpolated using cubic splines onto a homogeneous grid with a resolution of 2.0 mm isotropic. Relative B_1^+ and relative B_1^- were calculated by taking an arbitrary channel as reference and used as input to the algorithm.

To test the robustness of the reconstruction method, complex white Gaussian noise was added to the simulated B_1. SNR of the B_1 maps was adjusted to 100 and 50 by modifying the standard deviation of the added noise.

2.5. Human study

All human experiment procedures were approved by the University of Minnesota Institutional Review Board (IRB) in accordance with federally approved guidelines.

Twelve volunteers (age 20–62) participated in the study at 7 T MRI scanner (Siemens, Erlangen, Germany) equipped with a customized 16-channel stripline transceiver array [32]. Paddings were used to ensure that the head was positioned in the center of the coil, and to restrict head motion during the experiment. The thickness of the paddings was adjusted depending on head size to increase subject comfort. Each coil element was tuned and matched to minimize power reflection at the resonance frequency (297 MHz). The coil elements were interfaced with a customized transmit/receive switch to toggle between RF power amplifiers (16 × 1 kW, Communication Power Corporation, Hauppauge, USA) and receive signal amplifiers. B_1^+ magnitude of each channel was acquired using a series of gradient echo (GRE) images with one channel transmitting at a time in a small-flip-angle regime (FA ≤ 10°), combined with actual flip-angle imaging (AFI) of all channels transmitting in a static B_1^+ shim setting [34,35]. A second series of GRE images (one channel transmitting at a time) was obtained with a FA twice larger to obtain the relative phase between channels at a higher SNR. Whenever a single static B_1^+ shimming pattern covering the whole brain without RF voids could not be obtained, a second AFI was acquired with a complementary RF shimming pattern [36]. Proton density weighted relative B_1^- was acquired using a long TR (8 s) GRE. Both B_1^+ and B_1^- maps were acquired in 12 consecutive axial slices in a resolution of 1.5 × 1.5 × 3.0 mm^3. The entire B_1 acquisition typically took ~90 min, including: pilot B_1 acquisition, RF power calibration for each channel and multi-channel B_1^+ shimming (~20 min), two AFI maps (~20 min), small-FA GRE 8 averages (~23 min), large-FA GRE 4 averages (~11 min), and B_1^- mapping (~12 min). An example of B_1 mapping is shown in Fig. 1. By combining two complementary B_1^+ shims, singularities on individual B_1^+ maps were eliminated. Proton density in the measured B_1^- was estimated and removed using $\frac{\sum_Q |\rho B_{1,q}^-(x,y)|}{\sum_P |B_{1,p}^+(-x,y)|}$ based on symmetry between B_1^+ and B_1^-. After division of the proton density weighting, anatomical structures were not visually appreciable on the estimated B_1^- maps.

T_1-weighted (T1w) images were acquired by forming the ratio between a 3D magnetization prepared rapid acquisition gradient echo (3D-MPRAGE) sequence (TI = 1.5 s, TR = 3.5 s, TE = 2.26 ms, FA = 6°, 1 average for 5.5 min) and a 3D small-FA GRE sequence (TR = 327 ms, TE = 2.26 ms, FA = 4°, 1 average for 0.5 min) with a resolution of 0.75 × 0.75 × 3.0 mm^3. Forming this ratio eliminates receive B_1 profile, T_2^*, proton density, and mitigates the impact of transmit B_1 profile [37].

2.6. Image reconstruction

Relative B_1^+ and B_1^- were smoothed using a 5 × 5 × 3 Gaussian low-pass filter with a standard deviation of 1.2 × 1.2 × 0.8. Their spatial gradient and Laplacian were taken with 5 × 5 × 3 Savitzky-Golay (SG) filters based on the principle of local polynomial fitting [38,39]. Relative B_1^+ from all 16 channels were concatenated to produce a linear equation system which was then solved in a pixel-by-pixel fashion to yield B_1^+ phase gradient $\nabla\varphi_r^+$, as well as $g_+ = \frac{\partial \ln \varepsilon_c}{\partial x} + i\frac{\partial \ln \varepsilon_c}{\partial y}$. The calculated $\nabla\varphi_r^+$ was combined with $|B_1^+|$ to obtain absolute B_1^+, and used to calculate local EPs using the Helmholtz equation. Similarly, relative B_1^- from all 16 channels were concatenated to yield $\nabla\varphi_r^-$ and $g_- = \frac{\partial \ln \varepsilon_c}{\partial x} - i\frac{\partial \ln \varepsilon_c}{\partial y}$.

The spatial gradient strength of the Helmholtz conductivity from Eq. (9) was calculated and sorted in the ascending order. The top N voxels (N = 2, 10, 20, 50, 100, 500) with the smallest magnitude of local conductivity gradient, and with local EP values falling in the range of 0.3 S/m ≤ σ ≤ 3 S/m and $10\varepsilon_0 \le \varepsilon \le 100\varepsilon_0$, were chosen as seed points, since they are expected to be less affected by the large oscillations near tissue boundaries. All seeds were weighted equally when solving Eq. (10). The proposed approach is referred to as automated gradient based Electrical Properties Tomography (Aug-EPT) in the following text.

2.7. Data analysis

Generic brain tissue segmentation was performed using T1w images and the FAST function in FSL (FMRIB's Software Library, Oxford, UK) [40,41]. Three tissue types were specified: Gray matter (GM, including cortical GM and deep brain nuclei), white matter (WM) and cerebral-spinal fluid (CSF). Bias field correction was enabled to remove residual B_1 inhomogeneity. Partial volume estimation based on the mixture model of Gaussians was enabled, resulting in tissue fractions of each voxel. To minimize partial volume effects, a voxel was identified as a specific tissue type only if a fraction of 100% was detected. The central three consecutive slices from each subject were used for statistical analysis to avoid edge effects from the top and bottom slices.

3. Results

3.1. Numerical simulations

Simulation results are shown in Fig. 2. In the noiseless case, Helmholtz equation yields accurate EP values in the homogeneous part of the brain, yet artifact arises on tissue boundaries. Compared to the result using true $\nabla\varphi^+$ calculated directly from simulated absolute phase, the one using estimated $\nabla\varphi^+$ from Eq. (7) has broader transition artifacts due to the additional estimation step. In the noisy cases, Helmholtz results using estimated $\nabla\varphi^+$ show aggravated noise effect. The center of the brain is noisier due to its smaller B_1 compared to the peripheral as a result of RF attenuation. In all cases, Aug-EPT gives improved imaging quality with minimal boundary artifacts and noise contamination, especially for the case of SNR = 50. Nevertheless, low-frequency bias can be observed especially for permittivity map,

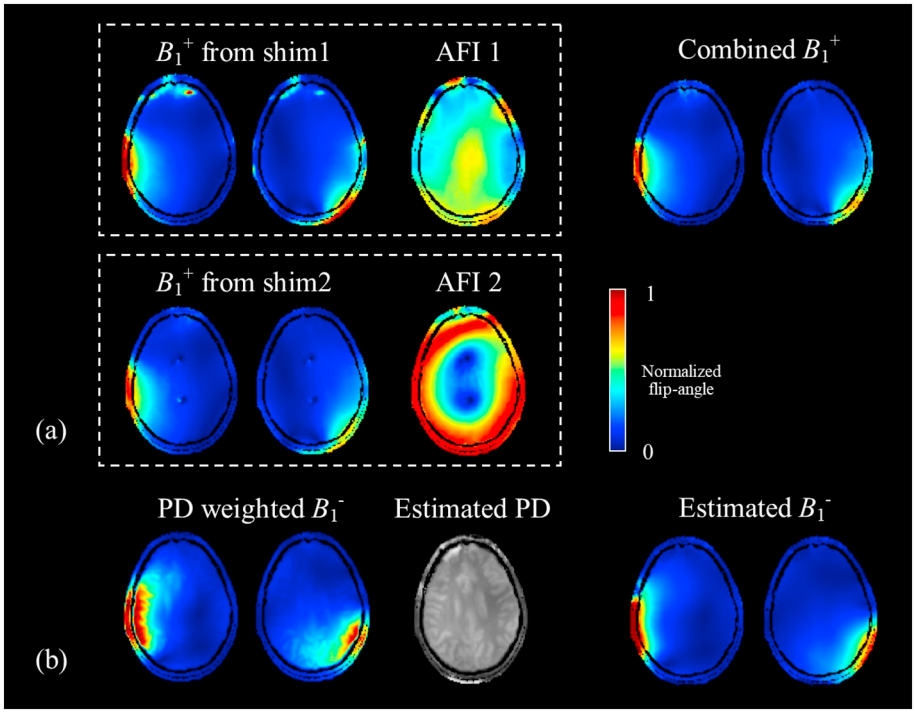

Fig. 1. B_1 maps from a representative human subject. (a) B_1^+ maps. Shown are B_1^+ from two channels (4 and 14) using two shim patterns (mapped by AFI) and their combination result. Color bar range is 0°–20° for single channel and 0°–100° for AFI. (b) B_1^- maps. Shown are raw proton density weighted B_1^- from two channels (4 and 14), estimated proton density, and de-weighted B_1^- maps.

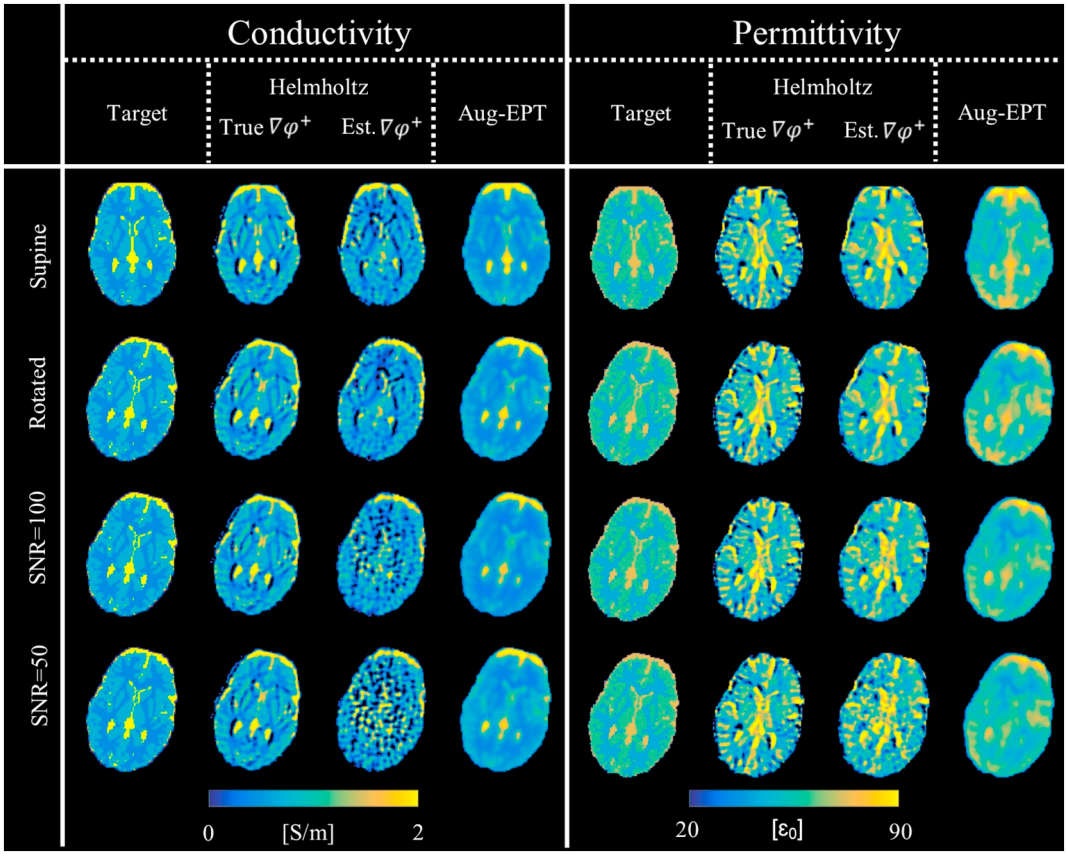

Fig. 2. Reconstructed conductivity and permittivity based on Helmholtz equation and Aug-EPT, using simulated B_1. From top to bottom row: Ella head model in supine position; After rotation about the central z axis by 15°; Noise added to adjust B_1 SNR to 100; Stronger noise added to adjust B_1 SNR to 50. From left to right column: Target EPs; Helmholtz reconstruction with true$\nabla\varphi^+$; Helmholtz reconstruction with estimated$\nabla\varphi^+$; Aug-EPT results.

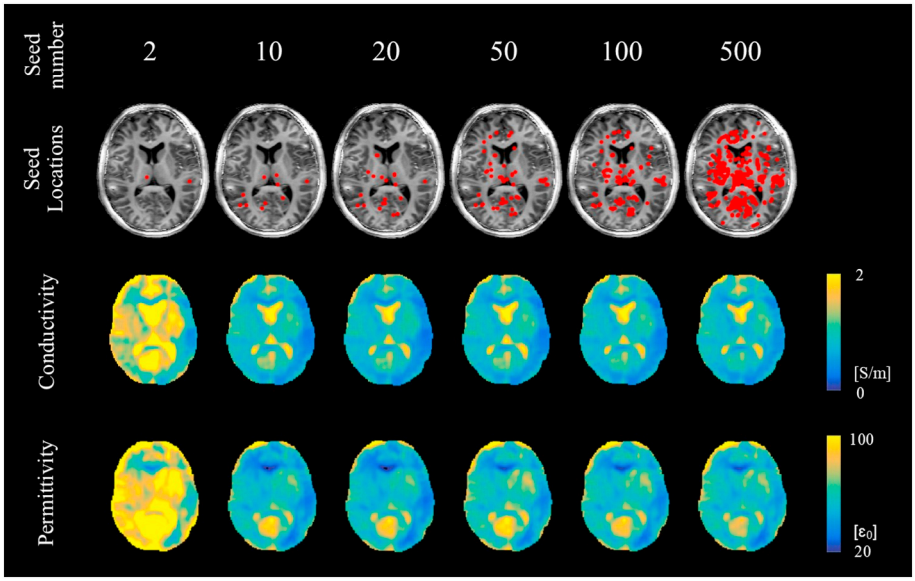

Fig. 3. Reconstructed conductivity and permittivity using Aug-EPT with different numbers of automatically selected seeds. Results are biased when using a small number of seeds, yet they converge when a large number is used.

presumably due to undesirable B_1 weighting. Lastly, none of the methods show significant dependency on head rotation.

3.2. In vivo human imaging

Fig. 3 shows reconstructed EPs of a representative subject using 2, 10, 20, 50, 100 and 500 seeds extracted from the Helmholtz result. The selected seeds are primarily distributed in brain tissues rather than CSF. This is because CSF has much higher EP values, leading to larger contrast deviations near tissue boundaries that are rejected by the algorithm. In addition, most seeds are co-localized with large homogeneous parts of brain tissue, such as thalamus, putamen, cortical gray matter and major white matter fibers, which is intended by the algorithm design. In cases where seed number is smaller than 20, both conductivity and permittivity deviate significantly from the expected values. The reconstruction results stabilize when > 20 seeds are chosen. The results do not demonstrate considerable sensitivity to the specific seed number chosen as long as > 20 are used. In the stabilized image, ventricles are depicted well, and gray matter with higher EPs can be better differentiated from white matter.

Using 100 seeds per slice, six consecutive slices from the same subject are shown in Fig. 4. For conductivity maps, good consistency across all slices is observed, and the contrast follows T1w images well. Permittivity images are less consistent, especially for the images near the top and bottom of the imaging slab. Note that low EP values are consistently observed in the corpus callosum of the brain compared to other white matter areas, which may be attributed to the larger macromolecule content in this highly myelinated structure [42].

gEPT methods are compared in Fig. 5. Conventional gEPT using one seed point in the putamen (red dot on T1w) yields EP maps similar to those by the proposed Aug-EPT method; however, reconstruction error increases in brain regions far away from the seed. For example, significant under-estimation of gray matter conductivity can be observed on the contralateral hemisphere. Moreover, conventional gEPT is sensitive to seed selection, as demonstrated in the second reconstruction trial using a different seed (blue dot on T1w) in cortical gray matter, which produces significantly elevated EP values. On the other hand, to examine the sensitivity of Aug-EPT to seed selection, the reconstruction

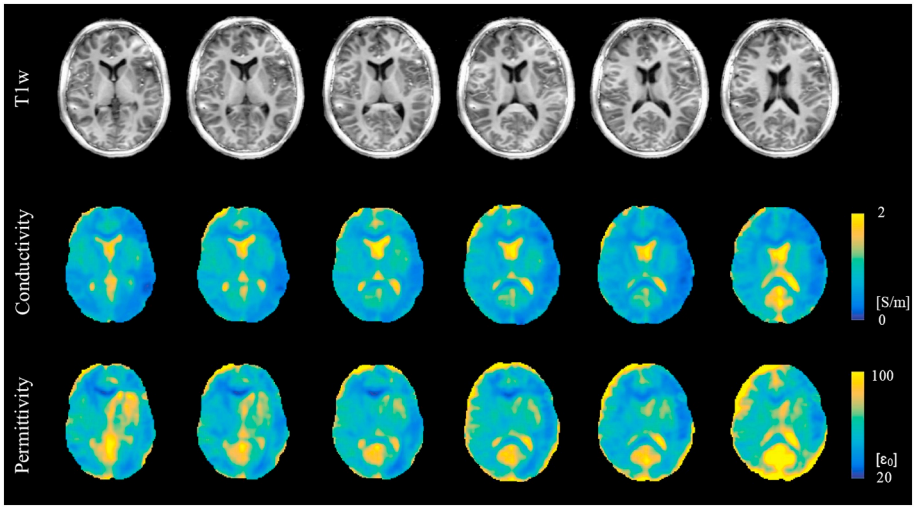

Fig. 4. Reconstructed results of six consecutive slices. Conductivity shows superior consistency compared with permittivity. Results close to the central slice of the imaging slab is superior to those from the edge slices due to absence of truncation effects in z-direction.

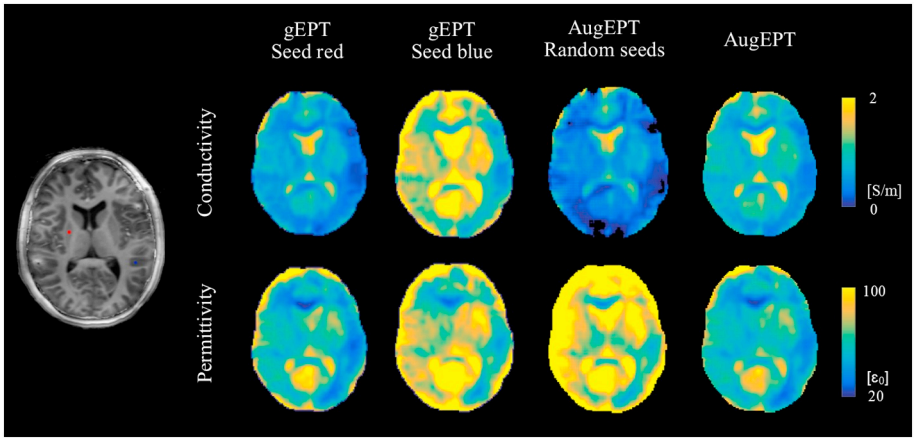

Fig. 5. Comparison of gEPT results. From left to right: T1w and seed locations for conventional gEPT; gEPT results using a single seed (red and blue, respectively); Aug-EPT results using 100 randomly chosen seeds; Aug-EPT results using 100 seeds chosen as proposed. (For interpretation of the references to color in this figure legend, the reader is referred to the web version of this article.)

was repeated using 100 randomly selected seeds. Compared to seeds chosen strategically using the proposed algorithm, random seeds introduce instability to the EP maps in terms of unpredictably deviating from the true values.

Inter-subject statistics are plotted in Fig. 6, using three imaging slices close to the center of the imaging slab. Inter-subject variation is considerably large when a small number of seeds are used, yet it converges when more than as 20 seeds are used. Paired *t*-test shows no statistical significance between the results using 50 and 100 seeds for both conductivity and permittivity of all three brain compartments. The comparison between reconstructed EPs and *ex vivo* EP values reported in the literature consistently shows a clear discrepancy. The *in vivo* data show higher conductivity in gray matter and white matter, and lower conductivity in cerebral-spinal fluid compared to *ex vivo* values. The permittivity values obtained from these two approaches show relatively smaller discrepancies, with $< 15\%$ difference for all brain compartments.

Reconstructed EPs in each brain compartment of each subject are shown as bars in Fig. 7. The quantitative statistics are reported and analyzed together with other EPT work in the following section.

3.3. Comparison to literature values

In vivo brain imaging results from healthy volunteers using EPT methods are summarized in Table 1 for conductivity and Table 2 for permittivity. Compared to a recently published review [43], this summary focuses on imaging results of normal brain, and categorizes data based on the B_1 type (magnitude, phase or complex) and EPT type (Helmholtz equation or heterogeneous model) used in each study.

The data generally follow the theory that conductivity increases with field strength (thus the RF frequency of interest). For white matter and gray matter, most *in vivo* studies report elevated conductivity compared to the *ex vivo* probed results at the corresponding frequency; however, for cerebral-spinal fluid, the results are somewhat mixed. Note that for conductivity calculation using only B_1 phase, it is assumed that B_1 magnitude is homogeneous, which theoretically leads to underestimation of B_1 spatial variation and conductivity itself. Also worth noting is that gEPT uses gray matter EPs reported in Gabriel et al. [20] as *a priori* information, which partially explains its higher similarity to the *ex vivo* results. For the data obtained in this study, GM and WM show significantly larger *in vivo* conductivity compared to their corresponding *ex vivo* values, while CSF has lower *in vivo* conductivity compared to its *ex vivo* measurement ($p < 0.001$ for all).

The scarcity of permittivity data compared to conductivity is attributed to the requirement for absolute B_1 magnitude, which necessitates a dedicated B_1 mapping sequence. On the other hand, the detection power of permittivity at lower field than 7 T is much reduced due to the relatively flat profile of B_1, rendering it more difficult to fit to the

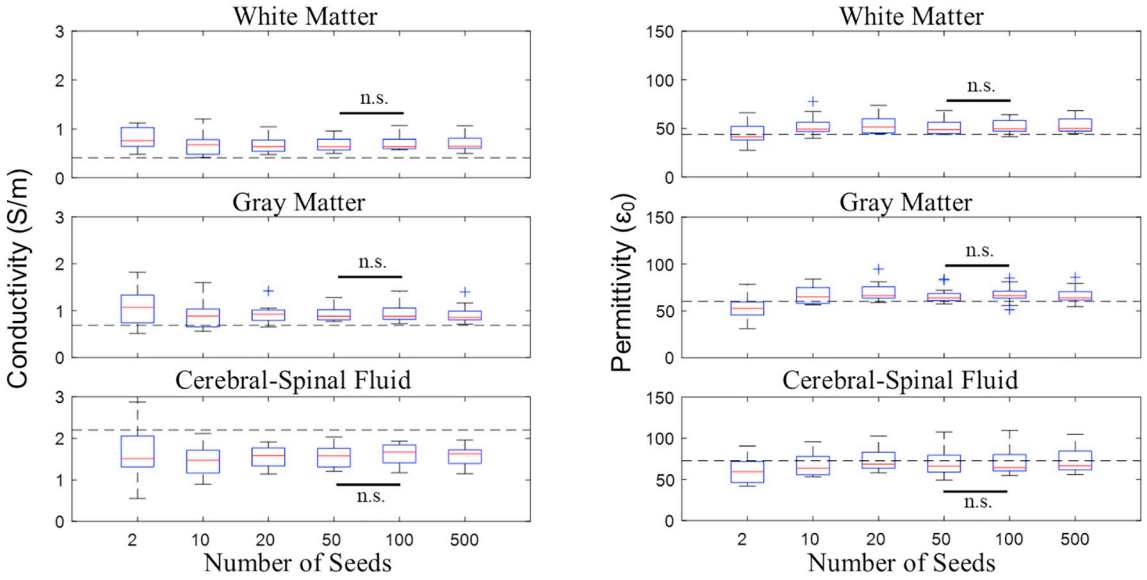

Fig. 6. Box plots of mean reconstructed EP values of three brain compartments over subjects with various seed numbers. Dashed line denotes *ex vivo* EP values of the corresponding brain tissue at 298 MHz from [2]. Paired *t*-test was performed between results using 50 and 100 seeds in all three types of tissues. n.s. not significant.

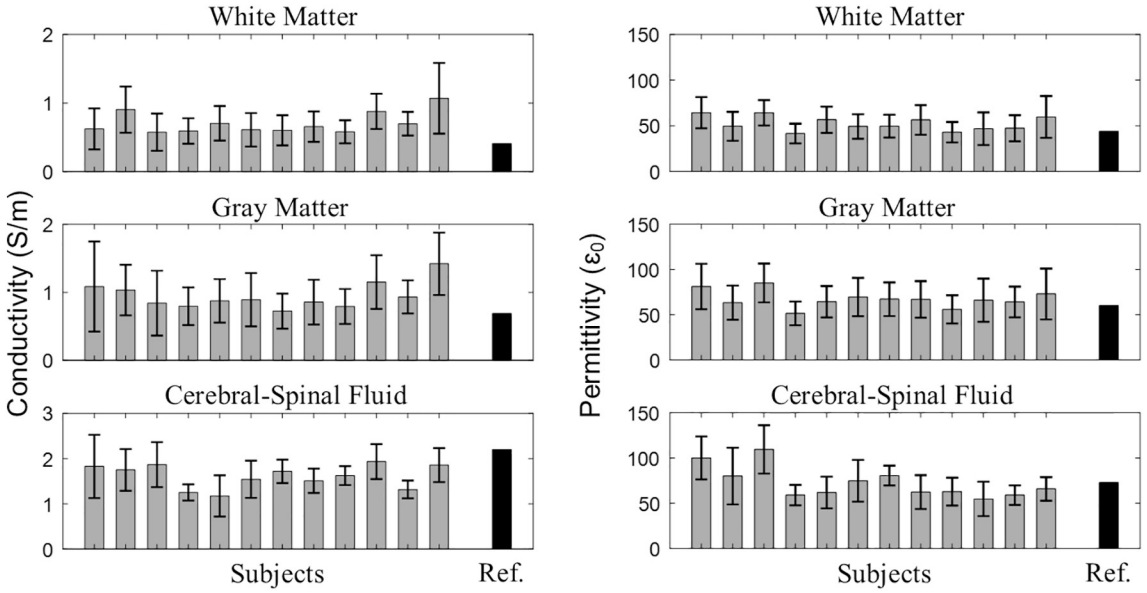

Fig. 7. Bar plots of reconstructed EP values of brain tissues in individual subjects. Data are shown as mean ± standard deviation inside region of interest. Black bars denote *ex vivo* EP values of the corresponding brain tissue at 298 MHz from [2].

RF wave equations. For the available data at 7 T, it is observed that the relative difference between *in vivo* and *ex vivo* values are smaller, typically < 15%.

4. Discussion

We have proposed a new strategy to retrieve human brain EPs using a multi-transceive RF array at 7 T MRI based on gEPT without the need of manually choosing seed points during the reconstruction, therefore avoiding potential user-dependent reconstruction bias. Results of numerical simulations and experiments involving 12 subjects demonstrate the consistency of the approach when > 20 seeds are used. This technique holds promise to facilitate an objective and fully automated gEPT approach for *in vivo* imaging of the human brain. Using this technique to collect the to-date largest *in vivo* data set of brain EPs in volunteers, a systematic deviation was observed when compared with *ex vivo* brain EPs values reported in the literature. These differences confirm previous findings in other EPT studies with a smaller subject number. Our result may be useful to identify abnormal EP values in brain disease, as well as to provide realistic values in numerical models for electromagnetic simulation of the human brain.

Using the proposed Aug-EPT technique, consistent EP values of brain tissues are observed in our cohort of 12 human subjects, which are close yet not statistically equal to the *ex vivo* values reported in the widely referenced work by Gabriel et al. at Larmor frequency [20]. Specifically, *in vivo* conductivity of GM and WM is significantly higher, and that of CSF is lower. The same trend can be noticed for permittivity, but to a much less extent. The results agree with an *in vivo* probe measurement study performed on swine [50]. The higher EPs in GM and WM can potentially be ascribed to the *in vivo* nature of EPT *versus ex vivo* probe measurements. For the *in vivo* imaging case, blood infiltration in brain tissues could lead to conductivity increase, while causing minimal effects on permittivity [51]. Another source of discrepancy is the fitting of the *ex vivo* data to the mathematical model (Cole-Cole dispersion model). Retrieval of EPs at specific frequencies using this model gives an approximation to the actual measurement results, which are subject to fitting and interpolation errors. On the other hand, *in vivo* conductivity of CSF by EPT is smaller than the values

Table 1
Human brain conductivity values at relevant frequencies in literature. Data is grouped based on the associated B_0 field (operating RF frequency). The *ex vivo* measurement result is shown together with EPT results. "Phase" denotes phase-only approximation; "Complex" means both B_1 phase and magnitude are used; "Heterogeneous" means EP variation is accounted for in the central equation. Data are shown as mean ± standard deviation over subjects for studies having more than two subjects. One sample two-tailed *t*-test was performed between *in vivo* values obtained in this study and the corresponding *ex vivo* values.

B_0 (RF freq.)	B_1	EPT type	WM	GM	CSF	Subject number	Study
1.5 T	NA (probed *ex vivo*)		0.29	0.51	2.06	NA	[20]
(64 MHz)	Phase	Helmholtz	0.43 ± 0.15	0.72 ± 0.15	1.82 ± 0.37	6	[24,44]
	Complex	Helmholtz	0.39 ± 0.15	0.69 ± 0.14	1.75 ± 0.34	6	[24,44]
3.0 T	NA (probed *ex vivo*)		0.34	0.59	2.14	NA	[20]
(128 MHz)	Phase	Helmholtz	0.36 ± 0.05	0.68 ± 0.06	2.20 ± 0.13	3	[45]
	Phase	Helmholtz	0.45 ± 0.52	1.38 ± 1.70	1.65 ± 2.87	4	[46]
	Complex	Helmholtz	0.30	0.61	NA	1	[47]
	Phase	Heterogeneous	0.53	0.76	1.71	1	[48]
7.0 T	NA (probed *ex vivo*)		0.41	0.69	2.22	NA	[20]
(298 MHz)	Phase	Helmholtz	0.63	0.87	1.93	1	[49]
	Complex	Helmholtz	0.63 ± 0.05	0.81 ± 0.02	2.47 ± 0.04	3	[26]
	Complex	Heterogeneous	0.4, 0.5	0.7, 0.7	1.3, 1.5	2	[19]
	Complex	Heterogeneous	0.5	0.9	1.7	1	[36]
	Complex	Heterogeneous	0.70 ± 0.16***	0.95 ± 0.19***	1.61 ± 0.26***	12	This study

*** $p < 0.001$.

Table 2
Human brain permittivity values at relevant frequencies in literature. Data presentation is in a similar scheme to that of Table 1. "mag." denotes magnitude-only approximation of the Helmholtz equation. One sample two-tailed *t*-test was performed between *in vivo* values obtained in this study and the corresponding *ex vivo* values.

B_0 (RF freq.)	B_1	EPT type	WM	GM	CSF	Subject number	Study
1.5 T	NA (probed *ex vivo*)		67.8	97.4	97.3	NA	[20]
(64 MHz)	Mag.	Helmholtz	63 ± 66	91 ± 70	98 ± 20	6	[24,44]
	Complex	Helmholtz	72 ± 64	103 ± 69	104 ± 21	6	[24,44]
3.0 T	NA (probed *ex vivo*)		52.5	73.5	84.0	NA	[20]
(128 MHz)							
7.0 T	NA (probed *ex vivo*)		43.8	60.1	72.8	NA	[20]
(298 MHz)	Complex	Helmholtz	48.7 ± 3.5	64.3 ± 2.5	78.3 ± 1.5	3	[26]
	Complex	Heterogeneous	46, 44	60, 62	58, 73	2	[19]
	Complex	Heterogeneous	61	71	93	1	[36]
	Complex	Heterogeneous	52.3 ± 7.7**	67.2 ± 9.3*	72 ± 17 (n.s.)	12	This study

n.s. not significant.
** $p < 0.01$.
* $p < 0.05$,

reported by [20], yet it is in agreement with [50]. Nevertheless, EPs of CSF are expected to be underestimated by imaging because of the relatively scattered distribution that renders it sensitive to partial volume effects. Other confounding factors include pulsation of the CSF that affects the results differently depending on sequence implementation and subject physiology.

Consistent with previous *ex vivo* measurement results [52] and *in vivo* EPT [16], considerable intra-subject variation of each tissue, up to 30%, can be observed, potentially induced by the natural heterogeneity of tissues due to differences in blood infiltration and tissue microstructure [53,54]. This EP heterogeneity needs to be considered when determining the contrast of "normal" and malignant tissues. On the other hand, spatial heterogeneity of malignant tissues correlates to pathological features, such as necrosis, which may help with sensitivity and specificity of diagnosis and grading [29,55].

Considering the different physiology of in vivo versus ex vivo cases, natural heterogeneity of tissues, as well as the inter-subject variation due to body condition, it is expected that *in vivo* subject-specific EPs obtained by EPT can contribute to additional accuracy in electromagnetic modeling and management, which could be important especially for safety ensurance purposes, such as estimation of local heating in MRI exams [18]. Meanwhile, the diagnostic power of EPs should be examined considering the inter- and intra-subject heterogeneity, *i.e.*, whether the deviation of diseased tissue EPs is significant.

EPs as intrinsic physical properties of tissue may be indicative of chemical and physiological properties that are otherwise more difficult to obtain. For example, quantitative sodium imaging is promising to provide metabolic information [56], yet it requires separate electronics to acquire ^{23}Na signal at a different resonance frequency using MRI. Considering the abundance of ^{23}Na in the body, conductivity may be a good substitute that does not require additional hardware. Another potential application is the quantification of macromolecules in the brain using permittivity, *e.g.*, myelin quantification in the white matter. It has been known that tissue permittivity in the radiofrequency range correlates well with water content [57], and water fraction (or its counterpart macromolecular fraction) correlates with brain myelination [58]. However, literature that directly associates myelin with permittivity is lacking and further investigation is needed to confirm the correlation.

Despite that twelve is the largest subject population so far for *in vivo* brain EPT, it is still a relatively small number. It is expected that EPs from a larger population of volunteers will be reported to further solidify the findings of this study. Particularly, the subject population may be scaled up in retrospective studies using the phase-only assumption, in a fashion similar to [15]. With larger subject pool, it would also be interesting to explore the effects of age and sex on *in vivo* EPs, and eventually their impact on the accuracy of electromagnetic simulations.

5. Conclusion

The subjective process of assigning seed points in gradient-based EPT (gEPT) can be relieved by using Helmholtz equation to inform the reconstruction. Numerical simulations demonstrate the robustness of the proposed approach to noise contamination and head position. Consistent results are obtained *in vivo* in a group of 12 healthy subjects. This study as well as previous EPT studies synergistically support the notion that conductivity of white matter and gray matter is larger *in vivo* compared to *ex vivo* probe measurement results.

Acknowledgment

This work was supported by NIH R21 EB017069, R01 AT009263, R01 EB021027, R01 NS096761, RF1 MH114233, P30 NS076408, P41EB015894 and S10RR026783, and WM KECK Foundation. The authors thank Dr. Pramod Pisharaby and Dr. Catarina Saiote for assistance with T1w analysis, and Dr. Jiaen Liu for constructive discussions.

References

[1] Pethig R. Dielectric properties of biological materials: biophysical and medical applications. IEEE Transactions on Electrical Insulation 1984;EI-19:453–74. https://doi.org/10.1109/TEI.1984.298769.
[2] Gabriel S, Lau RW, Gabriel C. The dielectric properties of biological tissues: II. Measurements in the frequency range 10 Hz to 20 GHz. Phys Med Biol 1996;41:2251–69. https://doi.org/10.1088/0031-9155/41/11/002.
[3] Metherall P, Barber DC, Smallwood RH, Brown BH. Three-dimensional electrical impedance tomography. Nature 1996;380:509–12. https://doi.org/10.1038/380509a0.
[4] Mueller JL, Isaacson D, Newell JC. A reconstruction algorithm for electrical impedance tomography data collected on rectangular electrode arrays. IEEE Transactions on Biomedical Engineering 1999;46:1379–86. https://doi.org/10.1109/10.797998.
[5] Gao N, Zhu S, He B. A new Magnetic Resonance Electrical Impedance Tomography (MREIT) algorithm: RSM-MREIT algorithm with applications to estimation of human head conductivity. Phys Med Biol 2006;51:3067–83. https://doi.org/10.1088/0031-9155/51/12/005.
[6] Woo EJ, Seo JK. Magnetic resonance electrical impedance tomography (MREIT) for high-resolution conductivity imaging. Physiol Meas 2008;29:R1. https://doi.org/10.1088/0967-3334/29/10/R01.
[7] Xu Y, He B. Magnetoacoustic tomography with magnetic induction (MAT-MI). Phys Med Biol 2005;50:5175. https://doi.org/10.1088/0031-9155/50/21/015.
[8] Li X, Yu K, He B. Magnetoacoustic tomography with magnetic induction (MAT-MI) for imaging electrical conductivity of biological tissue: a tutorial review. Phys Med Biol 2016;61:R249. https://doi.org/10.1088/0031-9155/61/18/R249.
[9] Fear EC, Li X, Hagness SC, Stuchly MA. Confocal microwave imaging for breast cancer detection: localization of tumors in three dimensions. IEEE Transactions on Biomedical Engineering 2002;49:812–22. https://doi.org/10.1109/TBME.2002.

800759.
[10] Haacke EM, Petropoulos LS, Nilges EW, Wu DH. Extraction of conductivity and permittivity using magnetic resonance imaging. Phys Med Biol 1991;36:723–34. https://doi.org/10.1088/0031-9155/36/6/002.
[11] Katscher U, Voigt T, Findeklee C, Vernickel P, Nehrke K, Dossel O. Determination of electric conductivity and local SAR via B1 mapping. IEEE Trans Med Imaging 2009;28:1365–74. https://doi.org/10.1109/TMI.2009.2015757.
[12] Zhang X, Zhu S, He B. Imaging electric properties of biological tissues by RF field mapping in MRI. IEEE Trans Med Imaging 2010;29:474–81. https://doi.org/10.1109/TMI.2009.2036843.
[13] Liu J, Wang Y, Katscher U, He B. Electrical properties tomography based on B1 maps in MRI: principles, applications, and challenges. IEEE Transactions on Biomedical Engineering 2017;64:2515–30. https://doi.org/10.1109/TBME.2017.2725140.
[14] Katscher U, van den Berg CAT. Electric properties tomography: biochemical, physical and technical background, evaluation and clinical applications. NMR Biomed 2017;30:e3729https://doi.org/10.1002/nbm.3729.
[15] Shin J, Kim MJ, Lee J, Nam Y, Kim M, Choi N, et al. Initial study on in vivo conductivity mapping of breast cancer using MRI. J Magn Reson Imaging 2015;42:371–8. https://doi.org/10.1002/jmri.24803.
[16] Balidemaj E, de Boer P, van Lier ALHMW, Remis RF, Stalpers LJA, Westerveld GH, et al. In vivo electric conductivity of cervical cancer patients based on B1 maps at 3T MRI. Phys Med Biol 2016;61:1596. https://doi.org/10.1088/0031-9155/61/4/1596.
[17] Tha KK, Katscher U, Yamaguchi S, Stehning C, Terasaka S, Fujima N, et al. Noninvasive electrical conductivity measurement by MRI: a test of its validity and the electrical conductivity characteristics of glioma. Eur Radiol 2018;28:348–55. https://doi.org/10.1007/s00330-017-4942-5.
[18] Zhang X, Schmitter S, Van de Moortele P, Liu J, He B. From complex mapping to local SAR estimation for human brain MR imaging using multi-channel transceiver coil at 7T. IEEE Trans Med Imaging 2013;32:1058–67. https://doi.org/10.1109/TMI.2013.2251653.
[19] Liu J, Zhang X, Schmitter S, Van de Moortele P-F, He B. Gradient-based electrical properties tomography (gEPT): a robust method for mapping electrical properties of biological tissues in vivo using magnetic resonance imaging. Magn Reson Med 2015;74:634–46. https://doi.org/10.1002/mrm.25434.
[20] Gabriel S, Lau RW, Gabriel C. The dielectric properties of biological tissues: III. Parametric models for the dielectric spectrum of tissues. Phys Med Biol 1996;41:2271–93. https://doi.org/10.1088/0031-9155/41/11/003.
[21] Hoult DI. The principle of reciprocity in signal strength calculations—a mathematical guide. Concepts in Magnetic Resonance 2000;12:173–87. https://doi.org/10.1002/1099-0534(2000)12:4<173::AID-CMR1>3.0.CO;2-Q.
[22] van den Bergen B, Stolk CC, Van den Berg JB, Lagendijk JJW, Van den Berg CAT. Ultra fast electromagnetic field computations for RF multi-transmit techniques in high field MRI. Phys Med Biol 2009;54:1253. https://doi.org/10.1088/0031-9155/54/5/010.
[23] Wen H. Noninvasive quantitative mapping of conductivity and dielectric distributions using RF wave propagation effects in high-field MRI. Proc SPIE, San Diego, USA 2003:471–7. https://doi.org/10.1117/12.480000.
[24] Katscher U, Kim D-H, Seo JK. Recent Progress and future challenges in MR electric properties tomography. Comput Math Methods Med 2013;2013. https://doi.org/10.1155/2013/546562.
[25] van Lier ALHMW, Raaijmakers A, Voigt T, Lagendijk JJW, Luijten PR, Katscher U, et al. Electrical properties tomography in the human brain at 1.5, 3, and 7T: a comparison study. Magn Reson Med 2014;71:354–63. https://doi.org/10.1002/mrm.24637.
[26] Zhang X, Van de Moortele P-F, Schmitter S, He B. Complex B1 mapping and electrical properties imaging of the human brain using a 16-channel transceiver coil at 7T. Magn Reson Med 2013;69:1285–96. https://doi.org/10.1002/mrm.24358.
[27] Sodickson D, Alon L, Deniz C, Ben-Eliezer N, Cloos M, Sodickson L, et al. Generalized local Maxwell tomography for mapping of electrical property gradients and tensors. Proc. Intl. Soc. mag. Reson. Med. vol. 21. 2013. p. 3372. Salt Lake City, USA.
[28] Liu J, de Moortele PFV, Zhang X, Wang Y, He B. Simultaneous quantitative imaging of electrical properties and proton density from maps using MRI. IEEE Trans Med Imaging 2016;35:2064–73. https://doi.org/10.1109/TMI.2016.2547988.
[29] Wang Y, Shao Q, van de Moortele P-F, Racila E, Liu J, Bischof J, et al. Mapping electrical properties heterogeneity of tumor using boundary informed electrical properties tomography (BIEPT) at 7T. Magn Reson Med 2019;81:393–409. https://doi.org/10.1002/mrm.27414.
[30] Duan S, Xu C, Deng G, Wang J, Liu F, Xin SX. Quantitative analysis of the reconstruction errors of the currently popular algorithm of magnetic resonance electrical property tomography at the interfaces of adjacent tissues. NMR Biomed 2016;29:744–50. https://doi.org/10.1002/nbm.3522.
[31] Mandija S, Sbrizzi A, Katscher U, Luijten PR, van den Berg CAT. Error analysis of helmholtz-based MR-electrical properties tomography. Magn Reson Med 2017;80:90–100. https://doi.org/10.1002/mrm.27004.
[32] Adriany G, Van de Moortele P-F, Ritter J, Moeller S, Auerbach EJ, Akgün C, et al. A geometrically adjustable 16-channel transmit/receive transmission line array for improved RF efficiency and parallel imaging performance at 7 tesla. Magn Reson Med 2008;59:590–7. https://doi.org/10.1002/mrm.21488.
[33] Christ A, Kainz W, Hahn EG, Honegger K, Zefferer M, Neufeld E, et al. The virtual family—development of surface-based anatomical models of two adults and two children for dosimetric simulations. Phys Med Biol 2010;55:N23. https://doi.org/10.1088/0031-9155/55/2/N01.
[34] Van de Moortele PF, Snyder C, DelaBarre L, Adriany G, Vaughan JT, Ugurbil K. Calibration tools for RF shim at very high field with multiple element RF coils: From ultra fast local relative phase to absolute magnitude B1 + mapping. Proc. Intl. Soc. mag. Reson. Med. vol. 15. 2007. p. 1676. Berlin, Germany.
[35] Yarnykh VL. Actual flip-angle imaging in the pulsed steady state: a method for rapid three-dimensional mapping of the transmitted radiofrequency field. Magn Reson Med 2007;57:192–200. https://doi.org/10.1002/mrm.21120.
[36] Wang Y, Van De Moortele P-F, He B. CONtrast Conformed Electrical Properties Tomography (CONCEPT) based on multi-channel transmission and alternating direction method of multipliers. IEEE Trans Med Imaging 2019;38:349–59. https://doi.org/10.1109/TMI.2018.2865121.
[37] Van de Moortele P-F, Auerbach EJ, Olman C, Yacoub E, Uğurbil K, Moeller S. T1 weighted brain images at 7 Tesla unbiased for proton density, T2* contrast and RF coil receive B1 sensitivity with simultaneous vessel visualization. NeuroImage 2009;46:432–46. https://doi.org/10.1016/j.neuroimage.2009.02.009.
[38] Savitzky A, Golay MJE. Smoothing and differentiation of data by simplified least squares procedures. Anal Chem 1964;36:1627–39. https://doi.org/10.1021/ac60214a047.
[39] Lee S-K, Bulumulla S, Hancu I. Theoretical investigation of random noise-limited signal-to-noise ratio in MR-based electrical properties tomography. IEEE Trans Med Imaging 2015;34:2220–32. https://doi.org/10.1109/TMI.2015.2427236.
[40] Zhang Y, Brady M, Smith S. Segmentation of brain MR images through a hidden Markov random field model and the expectation-maximization algorithm. IEEE Trans Med Imaging 2001;20:45–57. https://doi.org/10.1109/42.906424.
[41] Smith SM, Jenkinson M, Woolrich MW, Beckmann CF, Behrens TEJ, Johansen-Berg H, et al. Advances in functional and structural MR image analysis and implementation as FSL. Neuroimage 2004;23(Suppl. 1):S208–19. https://doi.org/10.1016/j.neuroimage.2004.07.051.
[42] Aboitiz F, Scheibel AB, Fisher RS, Zaidel E. Fiber composition of the human corpus callosum. Brain Res 1992;598:143–53. https://doi.org/10.1016/0006-8993(92)90178-C.
[43] Hancu I, Liu J, Hua Y, Lee S-K. Electrical properties tomography: available contrast and reconstruction capabilities. Magn Reson Med 2019;81:803–10. https://doi.org/10.1002/mrm.27453.
[44] Voigt T, Katscher U, Doessel O. Quantitative conductivity and permittivity imaging of the human brain using electric properties tomography. Magn Reson Med 2011;66:456–66. https://doi.org/10.1002/mrm.22832.
[45] Gho S-M, Shin J, Kim M-O, Kim D-H. Simultaneous quantitative mapping of conductivity and susceptibility using a double-echo ultrashort echo time sequence: example using a hematoma evolution study. Magn Reson Med 2016;76:214–21. https://doi.org/10.1002/mrm.25869.
[46] Ropella KM, Noll DC. A regularized, model-based approach to phase-based conductivity mapping using MRI. Magn Reson Med 2016;78:2011–21. https://doi.org/10.1002/mrm.26590.
[47] Shin J, Kim M, Cho S, Kim DH. Fast spin echo imaging based EPT with k-space weighting via T2 relaxation (rEPT). IEEE Trans Med Imaging 2017;36:1615–25. https://doi.org/10.1109/TMI.2017.2684194.
[48] Gurler N, Ider YZ. Gradient-based electrical conductivity imaging using MR phase. Magn Reson Med 2017;77:137–50. https://doi.org/10.1002/mrm.26097.
[49] van Lier ALHMW, Brunner DO, Pruessmann KP, Klomp DWJ, Luijten PR, Lagendijk JJW, et al. B 1+ phase mapping at 7 T and its application for in vivo electrical conductivity mapping. Magn Reson Med 2012;67:552–61. https://doi.org/10.1002/mrm.22995.
[50] Peyman A, Holden SJ, Watts S, Perrott R, Gabriel C. Dielectric properties of porcine cerebrospinal tissues at microwave frequencies: in vivo, in vitro and systematic variation with age. Phys Med Biol 2007;52:2229. https://doi.org/10.1088/0031-9155/52/8/013.
[51] Semenov S, Huynh T, Williams T, Nicholson B, Vasilenko A. Dielectric properties of brain tissue at 1 GHz in acute ischemic stroke: experimental study on swine. Bioelectromagnetics 2017;38:158–63. https://doi.org/10.1002/bem.22024.
[52] Salahuddin S, Gioia AL, Elahi MA, Porter E, O'Halloran M, Shahzad A. Comparison of in-vivo and ex-vivo dielectric properties of biological tissues. 2017 international conference on electromagnetics in advanced applications (ICEAA) 2017. p. 582–5. https://doi.org/10.1109/ICEAA.2017.8065312.
[53] Gelman N, Ewing JR, Gorell JM, Spickler EM, Solomon EG. Interregional variation of longitudinal relaxation rates in human brain at 3.0 T: relation to estimated iron and water contents. Magn Reson Med 2001;45:71–9. https://doi.org/10.1002/1522-2594(200101)45:1<71::AID-MRM1011>3.0.CO;2-2.
[54] Li T-Q, van Gelderen P, Merkle H, Talagala L, Koretsky AP, Duyn J. Extensive heterogeneity in white matter intensity in high-resolution T2*-weighted MRI of the human brain at 7.0 T. NeuroImage 2006;32:1032–40. https://doi.org/10.1016/j.neuroimage.2006.05.053.
[55] Kim S-Y, Shin J, Kim D-H, Kim E-K, Moon HJ, Yoon JH, et al. Correlation between electrical conductivity and apparent diffusion coefficient in breast cancer: effect of necrosis on magnetic resonance imaging. Eur Radiol 2018:1–11. https://doi.org/10.1007/s00330-017-5291-0.
[56] Thulborn KR. Quantitative sodium MR imaging: a review of its evolving role in medicine. NeuroImage 2018;168:250–68. https://doi.org/10.1016/j.neuroimage.2016.11.056.
[57] Foster KR, Schepps JL, Stoy RD, Schwan HP. Dielectric properties of brain tissue between 0.01 and 10 GHz. Phys Med Biol 1979;24:1177. https://doi.org/10.1088/0031-9155/24/6/008.
[58] Yarnykh VL, Yuan C. Cross-relaxation imaging reveals detailed anatomy of white matter fiber tracts in the human brain. NeuroImage 2004;23:409–24. https://doi.org/10.1016/j.neuroimage.2004.04.029.